Chemical Engineering Science 152 (2016) 497–506

Contents lists available at ScienceDirect

Chemical Engineering Science

journal homepage: www.elsevier.com/locate/ces

Effects of the orifice to pipe diameter ratio on orifice flows

Feng Shan [a,*], Zhichun Liu [a], Wei Liu [a], Yoshiyuki Tsuji [b]

[a] School of Energy and Power Engineering, Huazhong University of Science and Technology, Wuhan 430074, PR China
[b] Department of Energy Engineering and Science, Nagoya University, Nagoya 464-8603, Japan

HIGHLIGHTS

- Regions in orifice flows are defined based on statistical quantities of flow field.
- Characteristic length and velocity scales for different regions are discussed.
- Lengths of the primary and secondary recirculation regions are nearly independent of β.
- Profiles of Reynolds stress in the shear layers near the orifice plate are independent of β.

ARTICLE INFO

Article history:
Received 5 January 2016
Received in revised form
27 May 2016
Accepted 20 June 2016
Available online 21 June 2016

Keywords:
Orifice flow
Particle image velocimetry (PIV)
Recirculation region
Separated flow
Shear layer

ABSTRACT

This study presents the effects of the orifice to pipe diameter ratio (defined as the β ratio) on the flow field behind a thin circular square-edged orifice plate. We adopted a planar particle image velocimetry (PIV) system using two side-by-side cameras to measure velocity fields of a large area covering the reattachment region. The core, recirculation, and axisymmetric shear-layer regions are first suitably defined, and the characteristic length and velocity scales in different regions are then determined. When the orifice step height and mean streamwise velocity at the vena contracta are selected as the characteristic length and velocity scale, respectively, the mean flow field in the recirculation region shows nearly no β-ratio dependence. When the orifice pipe radius and local maximum mean streamwise velocity in the core region are selected as the characteristic length and velocity scales, respectively, the local peak Reynolds stresses are found to be independent of the β ratio in the shear-layer region close to the orifice plate. However, a β-ratio dependence appears as the flow progresses, and the pipe wall increasingly affects the shear-layer region. Although the mean streamwise velocity profiles in the shear layer show self-similarity, the Reynolds stresses do not maintain a self-similar property, indicating that the normalized statistical quantities at different streamwise locations follow the same profiles in the transverse direction.

1. Introduction

Orifice flow is a typical separated internal flow of great theoretical and practical interest. It is typically unsteady and includes flow reversal, three-dimensional separation, and vortex formation and shedding. As shown in Fig. 1, the flow field is characterized by (1) an upstream recirculation region, (2) a core region, (3) a primary recirculation region, (4) a secondary recirculation region, (5) an axisymmetric shear-layer region, (6) a shear-layer reattachment region, and (7) a redevelopment region.

Orifices are widely used in flow metering because of their ruggedness, simple mechanical construction, and other known advantages (Shah et al., 2012). As a result, many studies have focused on understanding the properties of orifice meters to improve the accuracy of flow metering. A detailed literature review of the experimental and numerical research on orifice flow related to orifice metering before the 1990s is given in a dissertation on the three-dimensional flow through orifice meters (Nail, 1991). With regard to orifice metering, some studies have focused on obtaining the associated discharge coefficients (Reader-Harris, 2015) and pressure drops (Cioncolini et al., 2015). Computational fluid dynamics (CFD) tools are also widely used in modeling and analyzing orifice meters (Reis et al., 2014; Shaaban, 2014; Shah et al., 2012; Singh and Tharakan, 2015).

In addition, it is known that wall mass transfer is greatly enhanced downstream of an orifice (Takano et al., 2016). In the nuclear and fossil fuel industries, this is widely known as the

* Corresponding author.
E-mail address: shanfeng@hust.edu.cn (F. Shan).

http://dx.doi.org/10.1016/j.ces.2016.06.050
0009-2509/

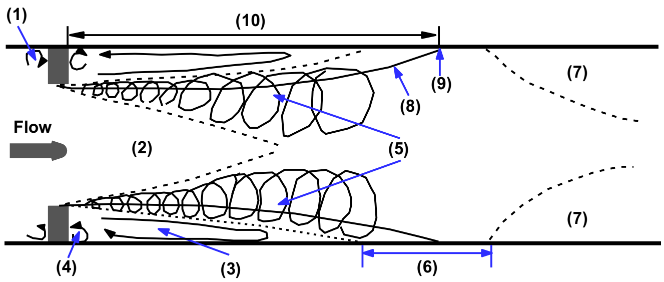

Fig. 1. Sketch of flow regions in orifice flow: (1) upstream recirculation region; (2) core region; (3) primary recirculation region; (4) secondary recirculation region; (5) axisymmetric shear-layer region; (6) reattachment region; (7) redevelopment region; (8) mean reattachment streamline; (9) mean reattachment point; (10) reattachment length x_r; the broken lines represent the imaginary boundaries of the core, shear layer, recirculation, and flow redevelopment regions; the chiral solid lines represent the vortex structures in the shear layer region.

flow-accelerated corrosion (FAC) process, which can result in the thinning and weakening of a pipe and lead to premature component failure (Fujisawa et al., 2015a; Fujisawa et al., 2015b). Over the past few decades, many severe accidents due to FAC have occurred in nuclear power plants and in the fossil fuel industry. Several studies have been conducted on FAC downstream of an orifice (Ahmed et al., 2012; El-Gammal et al., 2012; Hwang et al., 2009). Several factors, such as the turbulence levels, wall shear stress, and pressure, have been attributed as responsible for the enhanced wall mass transfer (El-Gammal et al., 2012). However, the flow mechanisms responsible for FAC downstream of orifices are still far from well understood. In addition to engineering and industrial applications, it is worth pointing out that orifice flow is also important in physiological research (Amatya and Longmire, 2010) and in micro-electrochemical systems (Mishra and Peles, 2005).

The study on effects of orifice to pipe diameter ratio (β ratio) has dated back to the 1930s. Johansen experimentally determined the discharge coefficients for sharp-edged circular orifices and conducted flow visualization up to a Reynolds number of 5.7×10^4 for several orifices possessing different β ratios and a constant thickness (Johansen, 1930a, b). Morrison et al. (1990; 1995) studied in detail the β ratio, swirl, axisymmetric flow distortion, and the Reynolds number dependence of wall pressure in orifice meters. The mean and turbulent flow fields both upstream and downstream of an orifice plate have been measured at a relatively fine spatial resolution for several β ratios (DeOtte et al., 1991; Morrison et al., 1993) using a 3D laser Doppler anemometry (LDA) system. Kumar et al. (2012) studied the influence of β ratio on cavity bubbles. El-Gammal et al. (2012) and Ahmed et al. (2012) numerically studied the effects of β ratio on the mass transfer rate behind the orifice. Although studies on the effects of β ratio are extensive, to the best of the authors' knowledge, no attempts have been made to determine the characteristic length and velocity scales in different regions of orifice flows. Therefore, the first research objective of the present study is to determine the characteristic velocity and length scales in different regions of orifice flows by measuring the flow field for a series of β ratios. It is believed that flow physics, such as the location of the vena contracta and characteristic length and velocity scales in orifice flow, are very interesting for researchers and engineers in the study of flow metering, particularly the effects of the β ratio on these flow physics. In addition, it is cumbersome and time-consuming to experimentally determine many β ratios. Therefore, researchers and engineers usually rely on CFD to determine the effects of the β ratio. In this case, validation of the computational code using experimental data becomes extremely important; however, these experimental data are very scarce. Therefore, the second research objective is to provide detailed experimental data for the validation of numerical code of orifice flows.

The rest of this paper is organized as follows. Section 2 describes the experimental setup. Section 3 presents the uncertainty quantification of the experiments. Section 4 presents the main results and discussions. Section 5 presents the conclusions.

2. Experimental setup

Fig. 2 shows the sketch of the whole flow loop. The size of the tank was approximately $1.8\text{m}\times1.6\text{m}\times1.4\text{m}$, and the inner diameter of the piping system was 46 mm. The loop was driven by a centrifugal pump, whose rotating speed was controlled by an inverter. Major changes of the flow rate were controlled by the inverter, and minor changes of the flow rate were adjusted by a flow control unit. The test section was made of Plexiglas to ensure the optical transparency of the flow field. The test section with an orifice inside was interchangeable and was connected to the loop by flanges. The inner surface of the two flanges connecting the test section and the flow loop were mounted flush to make sure that the disturbance on the flow could be neglected.

The Reynolds number based on the pipe diameter and cross-sectional mean velocity is 25,000. The working fluid is pure water whose physical properties can be easily obtained from literature. The fluorescent particles (Fluostar is commercially available from Kanomax) with mean diameters of 15 μm and density of 1.1 g/cm^3 were seeded to the water. Both the diameter and density of the seeding particles are suitable for PIV measurements in water according to the theoretical analyses (Adrian and Westerweel, 2010). By trial and error, the number of seeding particles suitable for the present study is determined from the number of particle images. We ensured that more than 10 particle images were obtained in each final interrogation size from previous theoretical analysis performed by other researchers (Keane and Adrian, 1992). This resulted in approximately 1.5 g particles in the 1 m^3 water used in our experiment.

According to the empirical equations for entrance length to achieve fully developed pipe flow in White (2011), approximately 20 times the pipe diameter is necessary to achieve fully developed pipe flow when Re=25, 000. The length of the straight pipe upstream of the orifice plate was 3400 mm (approximately 74 times the pipe diameter) to ensure fully developed pipe flow upstream of the orifice plate. In addition, we verified the fully developed

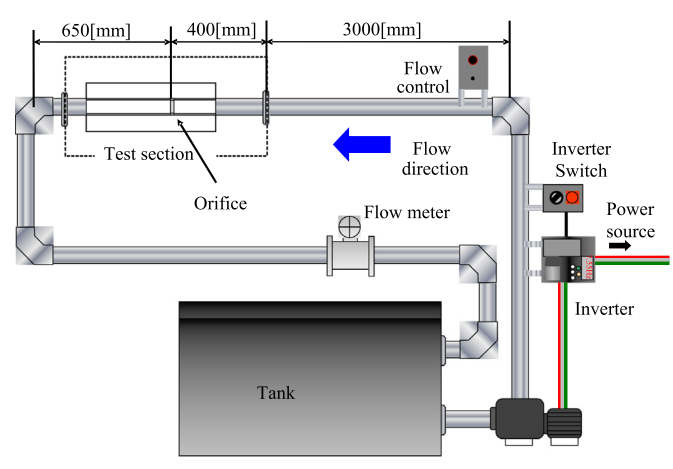

Fig. 2. Sketch of the flow loop.

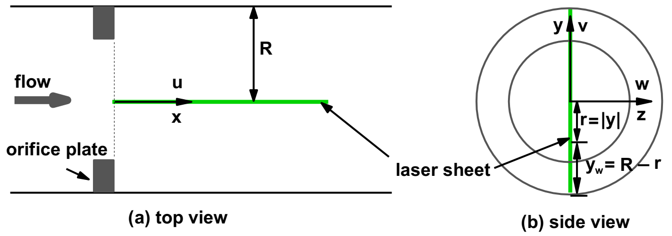

Fig. 3. Definition of the coordinate system and velocity components: $R \equiv D/2$ is the pipe radius; y=0 is the pipe center; $r = |y|$ is the distance from the pipe center, and y_w=$R - r$ is the distance from the pipe wall.

pipe flow condition by measuring the flow field in a test section with no orifice inside (i.e., a test section of a straight pipe). A satisfactory agreement was found between our results and previous results. However, the comparison is not shown here for brevity.

The coordinate system (x, y, z) employed for the axisymmetric orifice flow, in addition to the laser sheet position (the PIV measurement plane), is shown in Fig. 3, in which x, y, and z represent the streamwise, vertical, and spanwise coordinates, respectively. The origin is at the pipe center. In this study, we ensured that the center of the laser sheet corresponds to the pipe central plane (z=0). The symbol r=|y| represents the distance from the pipe center (y=0), and $y_w = R - r$ ($R \equiv D/2$ is the pipe radius) represents the distance from the pipe wall, which is more convenient to use than the vertical coordinate, y, in describing the flow field near the pipe wall. The symbols u,v, and w represent the streamwise, vertical, and spanwise components of instantaneous velocity, respectively. In addition, in this study, we follow the conventional Reynolds decomposition of the velocity components; i.e. $u = U + u'$ $v = V + v'$, and $w = W + w'$, in which the upper case symbols represent the mean velocity, and the lower case symbols with prime superscripts represent the fluctuating values. The angle bracket "$< >$" in this paper represents ensemble averaging. For instance, $\langle u'u' \rangle$, $\langle v'v' \rangle$ and $\langle u'v' \rangle$ represent Reynolds stresses.

In this study, the β ratios were 0.41, 0.5, and 0.62. We employed a Lavision PIV system for the PIV measurements and velocity field calculation. The Lavision PIV system included two Imager Pro X 2M 14-bit CCD cameras (1600×1200 pixels with a square pixel size of $7.4 \times 7.4\ \mu m^2$) as well as a New Wave Research 15 mJ Nd: YAG double-pulse laser for generating the optical laser sheet (wavelength λ_L=532 nm). The 105 mm$f$/2. 8D AF Nikkor ($f^{\#}$=2.8) lenses were mounted on the cameras for side-by-side planar PIV measurements. We set the sampling frequency of the PIV recording system at 11 Hz. In this experiment, fluorescent particles, Fluostar, from Kanomax were seeded in water as the working fluid. The mean diameter of the fluorescent particles was 15 μm and the density was 1. 1 g/cm^3. To record only the fluorescent light reflected by the fluorescent particles, two long-pass filters (λ_L>580 nm) were mounted in front of the two lenses. For further details about fluorescent PIV recording, refer to Yagi et al. (2009). One of the three interchangeable test sections with thin circular square-edged orifice plate of different β ratios was mounted in the flow loop with flanges. We maintained the thickness of the square-edged orifice plates, l, to be constant at 5mm, whereas we changed the orifice β ratio. To reduce the optical distortion during PIV measurements, we surrounded the near upstream and downstream areas of the orifice with an acrylic water tank $10D \times 6D \times 6D$ in size.

Fig. 4 shows the planar PIV system with two cameras placed side-by-side. With this setup, we were able to visualize a large area without sacrificing spatial resolution. The two cameras

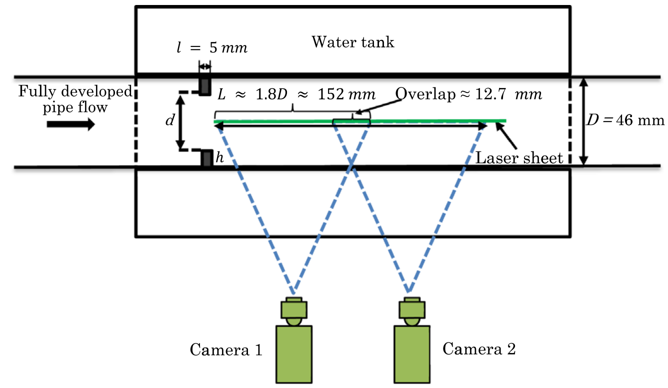

Fig. 4. Top view of the planar PIV setup using two cameras placed side-by-side (d = 18.9,23.0,25.5 mm and the corresponding h = 13.6,11.5,10.3).

simultaneously recorded particle images, and the information recorded by the two cameras can be stitched together to obtain a full instantaneous velocity field. In general, there are two methods for obtaining the full vector fields. In the first method, particle images from different cameras are first stitched to obtain the full image, and then, the full vector field is calculated (Cardesa et al., 2012). In the second method, the separate vector fields from all cameras are calculated first, and then, they are stitched to obtain the full vector field (Heerenbrink, 2011). In this study, we selected the latter method since stitching particle images is more complicated than stitching vector fields. The overlapped region in our experiment is approximately 15% of a single camera's image to ensure sufficient velocity vectors are available during vector stitching.

The particle images from each camera were first dewarped into real-world coordinates using the pinhole camera model (Hartley and Zisserman, 2000). Then, the multipass decreasing interrogation window cross-correlation method was used to calculate the velocity. The initial interrogation window size was 64×64 pixels with 50% overlap (three iterations), and the final interrogation window size was 32×32 pixels with 75% overlap (four iterations). In order to deal with the high-velocity-gradient shear layer in the orifice flow, we adopted the adaptive PIV method embedded in the commercial software packet Davis 8.3.0. The adaptive PIV method can automatically adjust the window size and shape according to

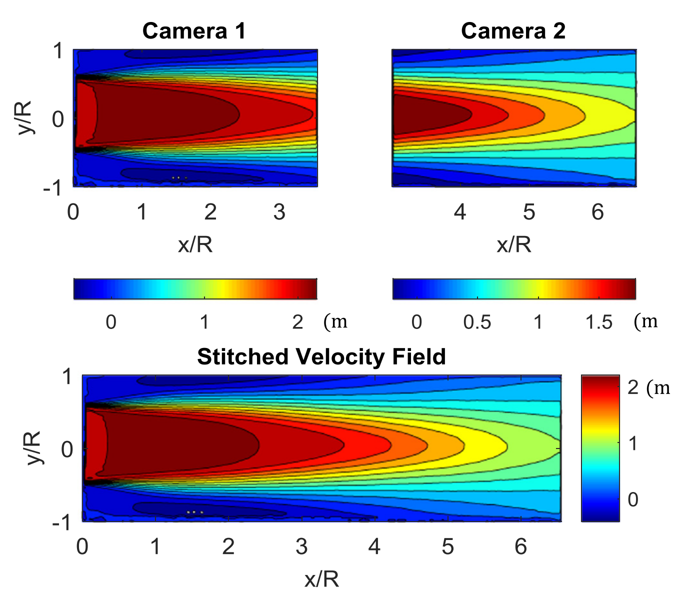

Fig. 5. Example of vector stitching of mean streamwise velocity field for β=0.62 and Re = 25,000.

velocity gradient and particle image quality, which can get more accurate results inside the shear layer (Wieneke and Pfeiffer, 2010). Finally, the vectors in the overlapped region were interpolated to obtain a full instantaneous velocity field. Fig. 5 shows an example of the vector stitching of mean streamwise velocity field. It can be seen that there is no huge discrepancy or sudden change in the full mean velocity field in the overlapped region of the two cameras after vector stitching. In addition, all statistical quantities based on those stitched instantaneous velocity fields in our later analyses are very smooth in the overlapped region.

3. Uncertainty quantification of the PIV measurements

Uncertainty quantification of PIV measurements is a very difficult process, though it has had rapid progress in recent years (Christensen and Scarano, 2015; Neal et al., 2015; Sciacchitano et al., 2015). Since a detailed discussion of the uncertainty quantification of PIV is beyond the scope of the present study, we very briefly provide the results of our uncertainty quantification in order to support our following discussions on the experimental results. To conduct our uncertainty quantification of PIV, we employed the correlation statistics method embedded in the commercial software package Davis 8.3.0, as proposed by Wieneke (2015). Note that the correlation statistics method has achieved reasonable success, as revealed in a collaborative work on PIV uncertainty quantification (Sciacchitano et al., 2015). Figs. 6 and 7 show as an example the root mean squares (RMS) of the uncertainty of streamwise velocity and vertical velocity for β=0.62, respectively. Fig. 6 demonstrates that the uncertainty of streamwise velocity is highly dependent on the property of the flow field itself. For instance, in the shear-layer region where the velocity gradient is extremely large, the uncertainty of the flow field is also very large (above 0.1 m/s); however, given the fact that the velocity magnitude is also very large, this large uncertainty is acceptable. Such results are unsurprising since, as is well known, the high-velocity-gradient shear layer is very challenging for PIV.

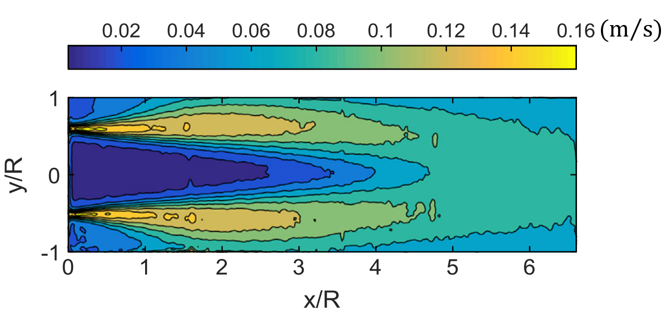

Fig. 6. Root mean square (RMS) of uncertainty of instantaneous streamwise velocity for β=0. 62.

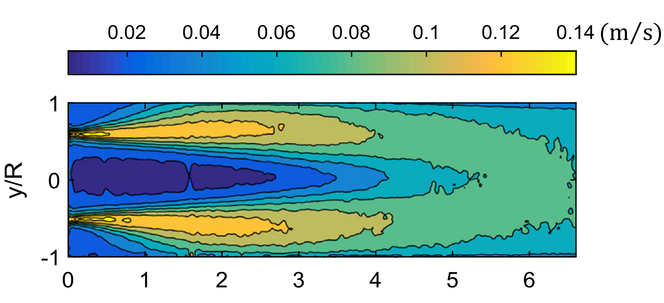

Fig. 7. RMS of uncertainty of instantaneous vertical velocity for β=0. 62.

Meanwhile, the uncertainty in the core region is very small, where the flow is very stable. The uncertainty in the recirculation region ranges from 0.04 m/s (approximately 0.2 pixel/s) to 0.1 m/s (approximately 0.5 pixel/s). The range of the RMS errors in the present study are consistent with those of some recent publications using a similar double-pulse PIV technique (Sciacchitano et al., 2013; Wieneke, 2015). Therefore, we believe that the data in the present study is acceptable. The uncertainty profile of vertical velocity as shown in Fig. 7 is similar to that shown in Fig. 6, only with a lower magnitude. Although it is also very challenging to measure the flow field very close to the pipe wall, it is interesting to note that the uncertainty values very close to the pipe wall are not very large due to the use of fluorescent particles. The uncertainty values of the velocities for other two β ratios show similar profiles to those shown in Figs. 6 and 7; for brevity, they are not shown here.

4. Results and discussions

4.1. Definitions of the core, shear-layer, and recirculation regions

To help the discussions in the later sections, we first suitably define the core region (2), recirculation regions, including (3) and (4), and axisymmetric shear-layer region (5), as sketched in Fig. 1. We first define the shear-layer region since this will help in defining the core and recirculation regions. In a free or separated shear layer, the vorticity thickness δ_ω or maximum slope thickness δ_{ms} is often used to describe the thickness of the shear layer. Brown and Roshko (1974) expressed δ_ω as

$$\delta_\omega \equiv \frac{\Delta U}{(\partial U/\partial r)_{max}} = \frac{U_h - U_l}{(\partial U/\partial r)_{max}} \tag{1}$$

where U_h and U_l represent the local (in this study, local means that the streamwise position is fixed) maximum and minimum mean streamwise velocities, respectively, and ΔU is the difference between them. In other words, δ_ω is based on the intercept points of the maximum velocity gradient line, extrapolated to U_h and U_l (Bradshaw, 1978). In the case of orifice flow, U_l is negative upstream of the mean reattachment point, as shown in Fig. 1; whereas U_l is the mean streamwise velocity at the pipe wall (U_l=0) downstream of the mean reattachment point. δ_{ms} in a separated shear layer is quite similar to δ_ω (Cherry et al., 1984); the only difference is the use of U_h instead of ΔU in the numerator. The definition of δ_{ms} is

$$\delta_{ms} = \frac{U_h}{(\partial U/\partial r)_{max}} \tag{2}$$

Usually, these two definitions will not result in significantly different results, and the difference between δ_ω and δ_{ms} is only a measure of the ratio between U_h and ΔU. In our case, the reverse flow velocity U_l is not very large; therefore, similar results will be obtained irrespective of the chosen definition. δ_ω was selected in this study.

Fig. 8 shows a sketch of δ_ω and δ_{ms} as well as our definitions for the shear-layer top edge y_t, center y_c, and bottom edge, y_b, using the profile of the mean streamwise velocity, U, at x/R=1 for β=0.62 as an example. As can be seen from Fig. 8, the difference between δ_ω and δ_{ms} is nearly indistinguishable. On the basis of the concept of δ_ω, we define y_t and y_b as the intercept points of the maximum velocity gradient line extrapolated to U_h and U_l, respectively, and y_c as the intercept point of the maximum velocity gradient line with the half-velocity difference $(U_h - U_l)/2$.

Fig. 9 shows y_t, y_b, y_c, and several statistical quantities for different β ratios. The orifice step height, h, is denoted by a double arrow on the vertical axis. The three dash-dotted lines in each

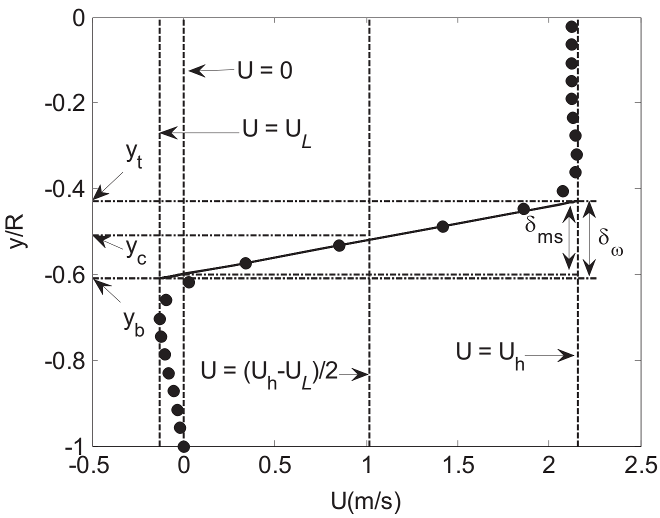

Fig. 8. Illustration of δ_ω, δ_{ms}, y_t, y_c, y_b using the profile of the mean streamwise velocity U at $x/R = 1$ for β=0.62: •, mean streamwise velocity profile; ——, tangent line passing the maximum velocity gradient position.

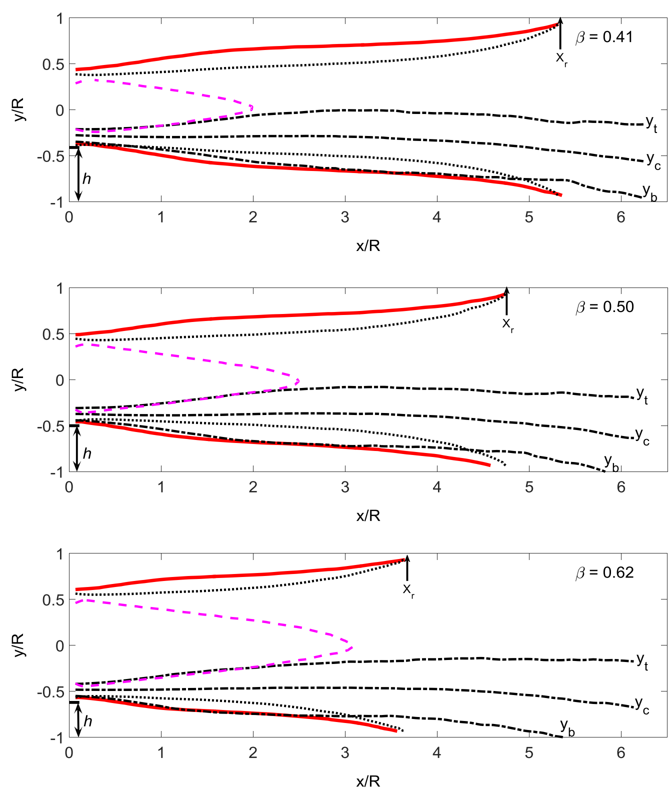

Fig. 9. Loci of statistical quantities for three β ratios: ——, stagnation lines U=0; - - - -, loci of $0.1\langle u'u'\rangle_{max}$, used to define the core region in this study; — · — y_t, y_c y_b; ...., mean reattachment streamline $\Psi = 0$; h, orifice step height.

graph represent y_t, y_c, and y_b, as introduced in Fig. 8. In separated internal flows such as axisymmetric sudden pipe expansion flow, one possible definition of the core region is the region in which the stagnation-pressure coefficient is greater than 0.99 (Devenport and Sutton, 1993). In this study, pressure measurements were not available; therefore, we defined the core region based on the velocity field. Specifically, the locus of 10% of the maximum Reynolds normal stress $\langle u'u'\rangle_{max}$ in the central region is defined as the core region, which is denoted by the magenta dashed lines in Fig. 9. This core region has low turbulence intensity from a statistical point of view. The determination of the ratio 10% is due to the loci of the defined core region agreeing reasonably well with the shear-layer top edges for all researched β ratios.

The definition of the recirculation region is relatively simpler; one good candidate for the definition is the stagnation lines $U = 0$ denoted by the red solid lines in Fig. 9. We define the recirculation region as the region bounded by the stagnation lines $U = 0$ and the pipe wall. The mean streamwise velocities on different sides of this line have different signs, which is probably the reason for the stagnation lines $U = 0$ also being called the separation line (Ruderich and Fernholz, 1986). In Fig. 9, we also plotted the mean reattachment lines, which are defined by the stream-function value $\Psi = 0$ and denoted by the black dotted lines. The stream-function value is calculated as the integration of the mean streamwise velocity from the pipe wall (U=0 and y_w=0) using the following equation:

$$\Psi\left(y_w\right) = \int_0^{y_w} U(y)dy \tag{3}$$

The stagnation lines U=0 and mean reattachment lines $\Psi = 0$ originate from the same locations close to the orifice plate and also intersect with the pipe wall at the same points, which are actually the mean reattachment points, as shown in Fig. 1. The decreasing trend of the reattachment length, x_r, with increasing β ratio can be seen in Fig. 9. The stagnation lines U=0 agree reasonably well with the shear-layer bottom edge from the outlet of the orifice plate until some location upstream of the mean reattachment point. We believe that the location where the stagnation lines U=0 start to differ from the shear-layer bottom edge is the beginning of the reattachment region (6) in Fig. 1. In summary, the recirculation region is defined as the region bounded by the stagnation lines U=0 and the pipe wall. After defining different regions in the orifice flow, we address the effects of β on the different regions defined in this section.

4.2. Effects of β on the core region

By examining the core region in Fig. 9, it can be seen that the length of the core region increases from approximately 2R to 3. 2R as β increases from 0.41 to 0.62. It should be noted that the length of the core region is determined by the position where the axisymmetric shear layer starts to interact. The axisymmetric shear layer forms at the edge of the orifice plate, develops as the flow progresses, and then interacts when its development is confined by the pipe wall. When the orifice to pipe diameter ratio increases from 0.41 to 0.62 (i.e., the diameter of the orifice throat increases), the space in the pipe center for the axisymmetric shear layer to develop increases, and it takes longer for the axisymmetric shear layer to start to interact. Therefore, the length of the core region increases with the increase of β.

In the core region of orifice flow, there is an important position called the vena contracta, which is defined as the point in a fluid stream where the diameter of the stream is at its minimum and fluid velocity is at its maximum, as shown in Fig. 10. At the vena

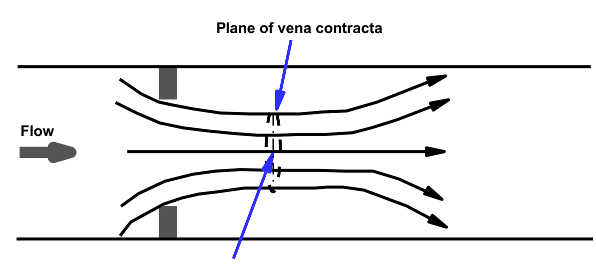

Fig. 10. Definition of the vena contracta and U_{max} in orifice flow.

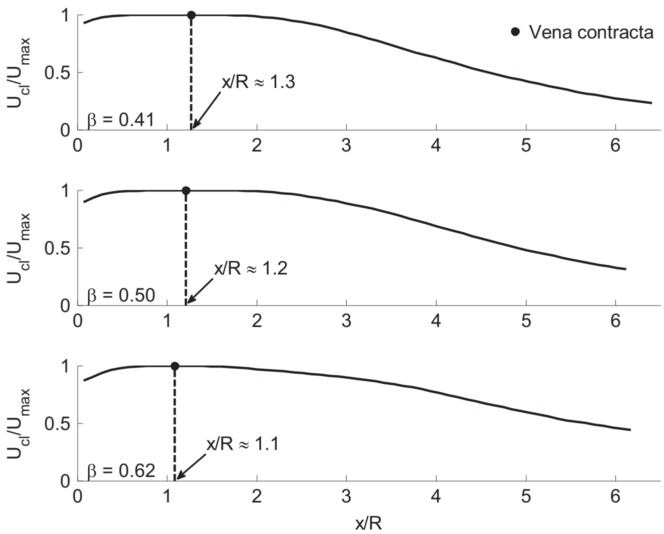

Fig. 11. Mean streamwise velocity at the pipe centerline and the vena contracta positions for different β ratios.

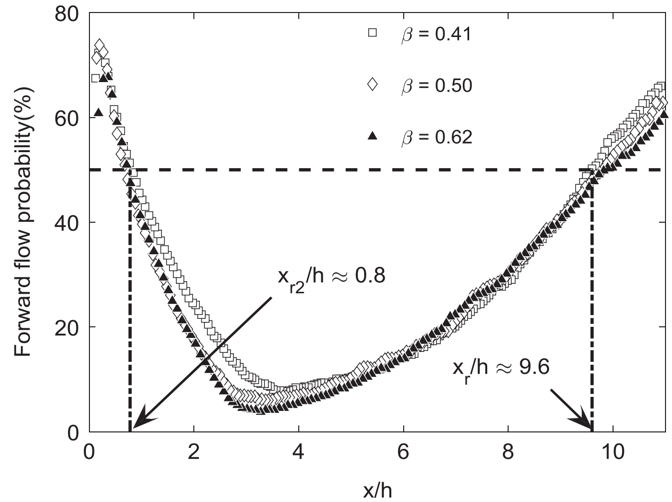

Fig. 12. Forward flow probability (FFP) at positions y_w=0.06R for different β ratios.

contracta, the mean streamwise velocity reaches its maximum, and it is defined as U_{max}. For further details on the vena contracta, refer to Massey and Ward-Smith (1998).

The position of the vena contracta can be determined by the peak position of the maximum mean streamwise velocity profile in the pipe centerline. Fig. 11 shows the mean streamwise velocity profile along the pipe centerline defined as U_{cl} and the vena contracta positions for different β ratios. The vena contracta moves slightly upstream with increasing β, as shown in Fig. 11. Because the flow field is very stable in the core region near the vena contracta, the uncertainty of the velocity field in that region is very small (Figs. 6 and 7). In other words, the velocity field near the vena contracta is very accurate. In addition, the uncertainty of the vena contracta position should be determined by the spatial resolution of the PIV technique. Near the vena contracta, where the flow is very stable (almost laminar flow), the spatial resolution of the PIV technique can be regarded as the grid size of the PIV measurement, which is 0.76 mm (approximately 0.03R) in this study. This grid size is smaller than the differences between the vena contracta positions (approximately 0.1R) for different β ratios. Therefore, it is believed that the slight difference in the vena contracta positions is due to the flow field, and not the experimental uncertainties. The vena contracta forms because the streamlines cannot change directions abruptly, which means they cannot closely follow the sharp edge of the orifice plate. Consequently, the mean streamlines start to contract at some distance upstream of the orifice plate and reach the smallest cross-sectional area at the vena contracta, followed by their expansion as shown in Fig. 10. When the orifice to pipe diameter ratio β increases from 0.41 to 0.62 (i.e., the orifice step height decreases), the distance from which the mean streamlines start to contract decreases, and the distance from which the streamlines start to expand also decreases. Therefore, the vena contracta moves upstream with increasing β.

4.3. Effects of β on the recirculation region

In separated flows, the forward flow probability (FFP) of the streamwise velocity at positions very close to the wall can be used to determine the lengths of the primary and secondary recirculation regions (Tihon et al., 2001). Fig. 12 shows the FFP of the streamwise velocity at approximately y_w=0.06R away from the wall for different β ratios. In Fig. 12, we can see that there are two positions where FFP is 50%, which correspond to the lengths of the primary and secondary recirculation regions, defined as x_r and x_{r2}, respectively. In addition, if the lengths are normalized by the orifice step height, h, these values are nearly independent of the β ratio. The recirculation region is formed because of the orifice plate. Therefore, if the orifice step height, h, is selected as the characteristic length scale to normalize the length of the primary and secondary recirculation region, the non-dimensional lengths of both the primary and secondary recirculation regions would become constant.

Fig. 13 shows the stagnation lines (U=0) and the maximum reverse flow positions defined as the locations that have the largest negative velocity in the recirculation region for the three orifices. The abscissa represents the streamwise length from the downstream surface of the orifice plate normalized by orifice step height, h, and the ordinate represents the distance from the pipe wall normalized by the orifice step height, h. We can see that the U=0 lines and maximum reverse flow positions agree reasonably well. The three long U=0 lines represent the separation lines between the primary recirculation region and the shear-layer region, and the dotted lines are the separation lines between the primary and secondary recirculation regions. It can also be seen that the maximum reverse flow positions are located at approximately x/h=4 (or $x/x_r \approx 0.42$) and $y/h \approx 0.2$, which is slightly upstream of

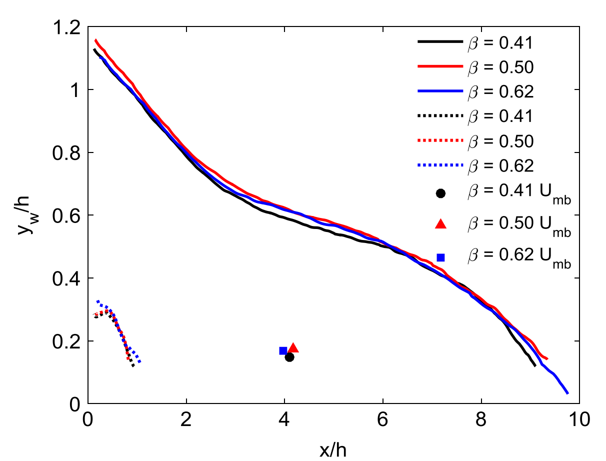

Fig. 13. Lines of mean streamwise U=0 and maximum mean reverse flow positions for three β ratios: solid lines represent separation lines of the primary recirculation and shear-layer regions; dotted lines represent separation lines of the secondary and primary recirculation regions; U_{mb} represents maximum reverse flow positions.

the center of the primary recirculation region. In addition, we found that if we use the streamwise velocity at the vena contracta U_{max} as the characteristic velocity scale, then the maximum mean reverse flow velocities in the recirculation region become nearly β-ratio independent. We already explained that orifice step height, h, is a characteristic length scale in the recirculation region, which is why nearly no β-ratio dependence is shown in Fig. 13.

It is worth pointing out that it is better to compare the physical quantities at the same non-dimensional locations normalized by h in the recirculation region. However, it is much easier to compare the physical quantities at the same dimensional locations in the PIV experiments if the same interrogation window size is selected. In this case, the non-dimensional location would become slightly different when it is normalized by h. For instance, in Fig. 13, when the same distance y_w=0.06R for three orifices is normalized by h, the non-dimensional locations vary from 0.10, for the case of β=0.41, to 0.16 for the case of β=0.62. It is believed that the discrepancy of non-dimensional locations for different β ratios is the main reason why some differences in the recirculation regions in Figs. 12 and 13 are observed.

4.4. Effects of β on the shear-layer region

4.4.1. Shear-layer growth rate

The growth of a shear layer can be measured in terms of the increase in δ_ω (as described in Eq. (1)). The shear-layer growth rates for three β ratios are shown in Fig. 14. Our results reveal that the shear layer develops in a similar way close to the orifice plate (upstream of $x/R \approx 2.5$) and then grows differently. The reason for this is that the shear layer forms hen the flow separates at the orifice lip, and then it develops freely close to the orifice plate before it is affected by the wall. However, as the flow progresses, the wall starts to confine the development of the shear layer, and a difference in shear layer growth occurs. In other words, there is a "turning point" when the effect of the wall appears. Similar turning points in the development of the shear layer were also reported in other separated internal flows (Devenport and Sutton, 1993) and outer flows (Castro and Haque, 1987).

4.4.2. Profiles of statistical quantities in the shear layer under a similarity coordinate

The similarity coordinate η for the analyses of the shear-layer region in the transverse direction is defined as follows:

$$\eta = \frac{(y - y_c)}{\delta_\omega} \tag{4}$$

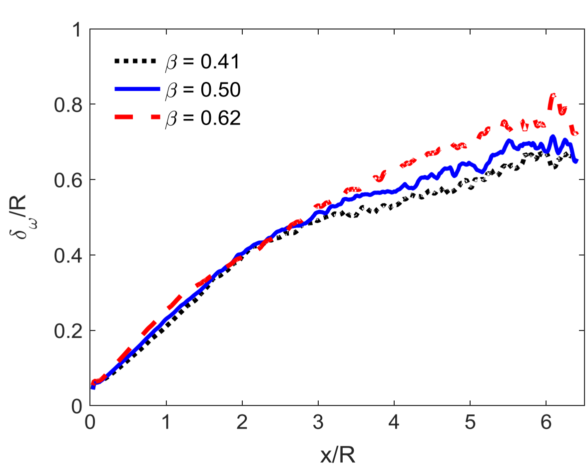

Fig. 14. Growth of the shear layer thickness δ_ω for three β ratios.

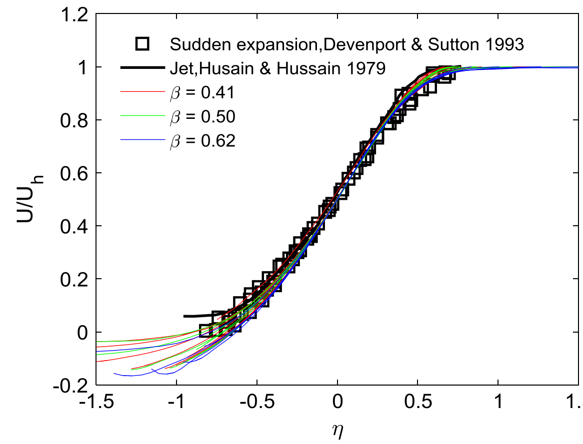

Fig. 15. Velocity profiles in similarity coordinates.

where y is the vertical coordinate defined in Fig. 3, y_c is the coordinate of the shear-layer center, as shown in Fig. 8, and δ_ω is the vorticity thickness defined in Eq. (2). It essentially means the vertical position from the shear layer center divided by local shear layer thickness. In other words, it is the non-dimensional vertical location from the shear layer center. Since the shear layer develops as the flow progresses, it is more meaningful to compare the physical quantities at the same non-dimensional vertical position. Consequently, similarity coordinates are widely used in the discussion of shear layers.

The self-similar properties of the mean velocity profiles of shear layers and developed jets have been a cornerstone of analysis in the field of separated internal flows (Bradshaw, 1978). In addition, self-similarity is a widely used concept in discussing the characteristics of the shear layers, for instance in (Castro and Haque, 1987; Ruderich and Fernholz, 1986; Wygnanski and Fiedler, 1969). Simply speaking, it means that the normalized statistical quantities at different stream-wise locations follow the same profiles in the transverse direction. Fig. 15 shows the mean streamwise velocity profiles for different β ratios in the shear-layer region plotted against the similarity coordinate, η. Note that not all the velocity profiles for orifice flows are shown for clear comparison. In Fig. 15, the local maximum mean streamwise velocity, U_h, is selected to normalize the velocity. It can be seen that the velocity profiles under similarity coordinates follow the profile similarly to an error function, which was also reported in other separated flows (Cherry et al., 1984; Ruderich and Fernholz, 1986). Inside the shear-layer region (similarity coordinate $-0.5<\eta<0.5$), it can be seen that the mean streamwise velocities follow the same profile, and the velocity data also agree very well with the data for the shear layer of the free jet (Husain and Hussain, 1979) and sudden pipe expansion (Devenport and Sutton, 1993). In the recirculation region ($\eta < -0.5$), there is a great divergence of the velocities. We already discussed that the characteristic length scale in the recirculation region is h. If the similarity coordinate, η, specially defined for the discussion of shear layers is used in the recirculation region, great divergence of velocity profiles would occur.

Fig. 16 shows $\langle u'u' \rangle$ normalized by U_h^2 in the shear-layer region for different β ratios. Similar results can be obtained for other components of Reynolds stress (not shown here for brevity). Even though the mean velocity for different β ratios follows similar profiles, the non-dimensional Reynolds stress only follows similar profiles in the first graph ($x/R = 1$) of Fig. 16. In fact, the Reynolds stress upstream of $x/R = 1$ for different β ratios follows similar profiles. This means that the turbulent structures upstream of $x/R = 1$ in the shear layers for different β ratios are similar. Downstream of $x/R = 1$, the Reynolds stress profiles for different β ratios differ, and no similar profile can be found irrespective of the

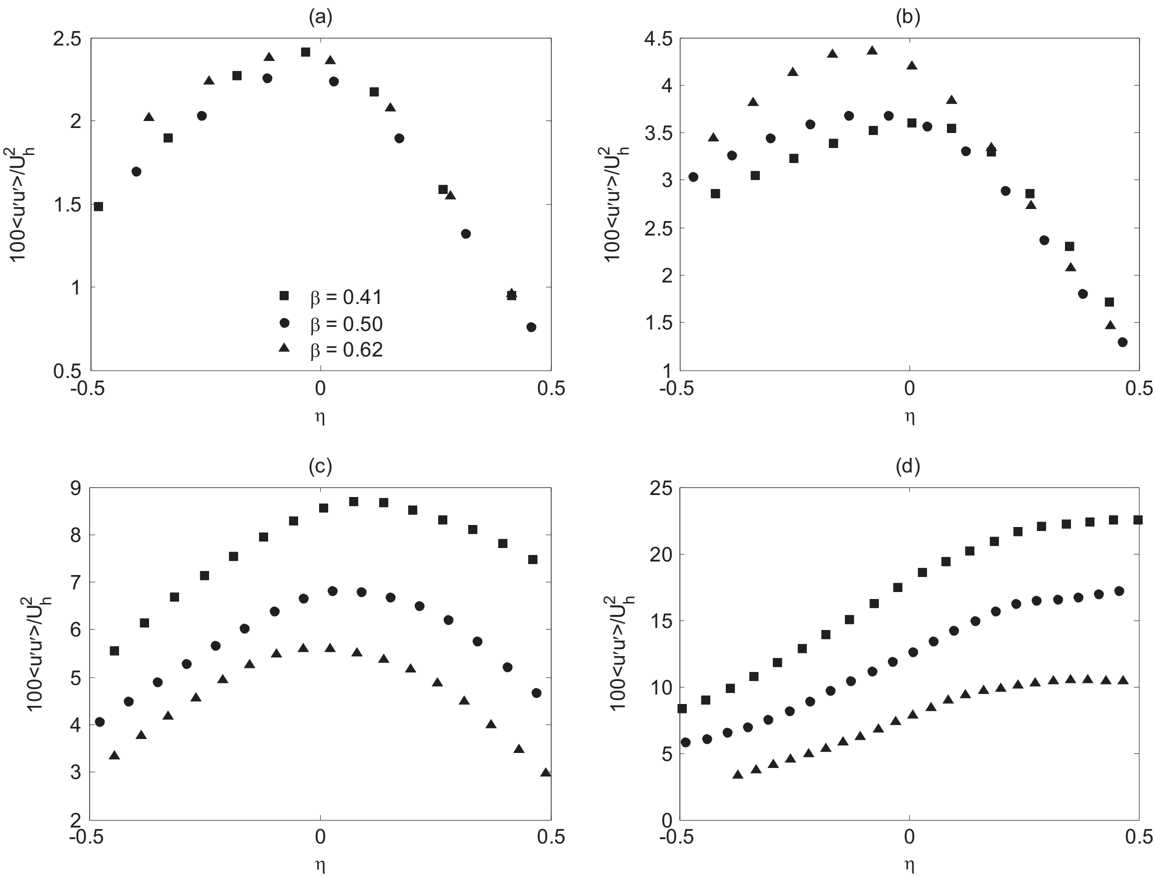

Fig. 16. $\langle u'u' \rangle$ profiles in the shear-layer region for different β ratios (a) x/R=1; (b) x/R=2; (c) x/R=3.5; (d) x/R=5.5.

parameters selected. Similar conclusions can be found for other components of Reynolds stress tensor such as $\langle v'v' \rangle$ and $\langle u'v' \rangle$.

Ruderich and Fernholz (1986) found that the mean and fluctuating quantities showed self-similar behavior in a short region upstream of reattachment. However, Castro and Haque (1987) argued that flow similarity is not an important property on the basis of their data for a separated shear layer behind a flat plate. According to our data for the separated shear layer of orifice flows, we conclude that the mean velocity profile is self-similar, as shown in Fig. 15. However, Fig. 16 suggests that the Reynolds stress profiles in the shear layer are not self-similar. Our findings extend the conclusion of Castro and Haque (1987) that the self-similar property is not a very useful concept in the turbulent shear layer of orifice flows.

4.4.3. *Local peak Reynolds stresses*

Fig. 17 shows the local peak Reynolds stresses normalized by U_h^2. Since the Reynolds shear stress $\langle u'v' \rangle$ could be negative, we compared the absolute values of the Reynolds shear stress for different β ratios. All local peak Reynolds normal and shear stresses for different β ratios follow a similar profile initially and then deviate. It is also worth pointing out that there is a region of decreasing Reynolds normal stresses, which is very close to the orifice plate. This phenomenon was also reported in the shear-layer region of axisymmetric backward-facing step flow (Hudy et al., 2007). The shear layer forms because of boundary layer separation at the lip of the orifice plate. In the very initial stage of the shear layer development, it can develop freely, and that is the reason that all Reynolds stresses in the shear layer at this initial stage show nearly no β ratio dependence. However, as the shear layer develops, it starts to feel the confinement of the pipe wall and can no longer develop freely. If the β ratio changes, the effect of the pipe wall also changes, and then the dependence of shear layer on β appears.

5. Conclusions

Different regions of orifice flows are suitably defined based on the statistical quantities of the flow field. The position of the vena contracta shows a slight β-ratio dependence. The mean streamwise velocity at the vena contracta, U_{max}, and the orifice step height are the characteristic velocity and length scales in the recirculation region. Many flow properties in the recirculation region, including the maximum mean reverse flow velocity and the lengths of the primary and secondary recirculation regions, show nearly no β ratio dependence. The axisymmetric shear layer initially develops freely close to the orifice plate; there, many physical quantities show nearly no β ratio dependence. As the flow progresses downstream, the core region disappears and effects of the wall become more and more important in the development of the shear layer; therefore, the statistical quantities show strong β ratio dependence. Although the mean velocity profiles in the shear-layer region exhibit self-similar properties and agree well with those of axisymmetric turbulent free jets and sudden pipe expansions, there is no self-similar property for the Reynolds stresses in the shear-layer region. This systematic experimental study on the effects of β ratios reveals that some typical velocity and length scales exist in orifice flows. In addition, there are some physical properties that will not change with β, which can be used

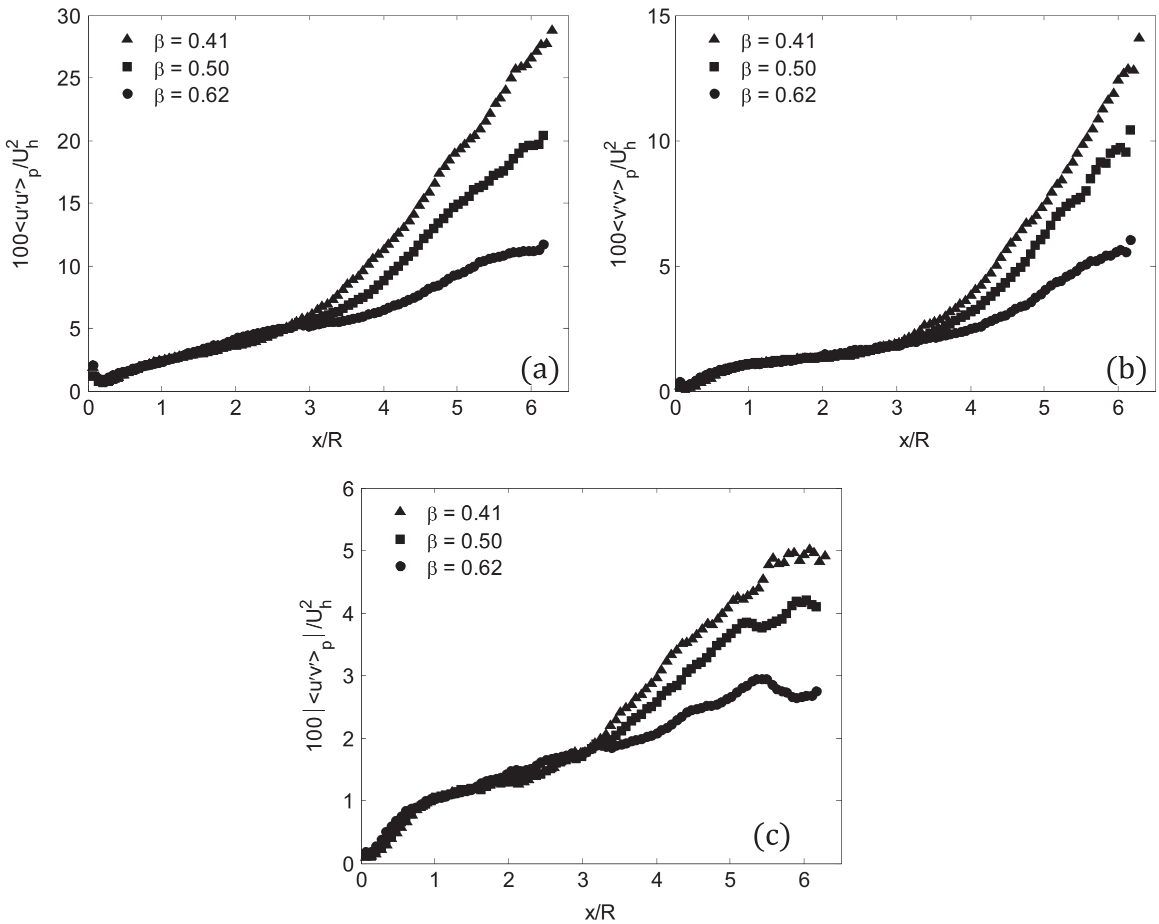

Fig. 17. Local peak Reynolds stress profiles in the streamwise direction: (a) $\langle u'u' \rangle_p$ normalized by U_h^2; (b) $\langle v'v' \rangle_p$ normalized by U_h^2; (c) $\left|\langle u'v' \rangle_p\right|$ normalized by U_h^2;.

to reduce the experimental efforts in orifice flows. Moreover, the detailed statistical quantities obtained by PIV can be used in verifying the numerical codes and turbulence modeling in orifice flows.

Acknowledgments

The work was supported by the National Key Basic Research Program of China (973 Program) (2013CB228302) and the National Natural Science Foundation of China (51376069). In addition, we want to thank Mr. Atsushi Fujishiro and Mr. Masashi Kano for their help in the experiments.

References

Ahmed, W.H., Bello, M.M., El Nakla, M., Al Sarkhi, A., 2012. Flow and mass transfer downstream of an orifice under flow accelerated corrosion conditions. Nucl. Eng. Des. 252, 52–67.

Amatya, D.M., Longmire, E.K., 2010. Simultaneous measurements of velocity and deformation in flows through compliant diaphragms. J. Fluids Struct. 26, 218–235.

Bradshaw, P., 1978. Topics in Applied Physics: Turbulence. 12. Springer-Verlag, Berlin.

Brown, G.L., Roshko, A., 1974. On density effects and large structure in turbulent mixing layers. J. Fluid Mech. 64, 775–816.

Cardesa, J.I., Nickels, T.B., Dawson, J.R., 2012. 2D PIV measurements in the near field of grid turbulence using stitched fields from multiple cameras. Exp. Fluids 52, 1611–1627.

Castro, I.P., Haque, A., 1987. The structure of a turbulent shear layer bounding a separation region. J. Fluid Mech. 179, 439–468.

Cherry, N.J., Hillier, R., Latour, M.E.M.P., 1984. Unsteady measurements in a separated and reattaching flow. J. Fluid Mech. 144, 13–46.

Christensen, K., Scarano, F., 2015. Uncertainty quantification in particle image velocimetry. Meas. Sci. Technol. 26, 070201.

Cioncolini, A., Scenini, F., Duff, J., 2015. Micro-orifice single-phase liquid flow: pressure drop measurements and prediction. Exp. Therm. Fluid Sci. 65, 33–40.

DeOtte Jr, R.E., Morrison, G.L., Panak, D.L., Nail, G.H., 1991. 3-D laser doppler anemometry measurements of the axisymmetric flow field near an orifice plate. Flow Meas. Instrum. 2, 115–123.

Devenport, W., Sutton, E., 1993. An experimental study of two flows through an axisymmetric sudden expansion. Exp. Fluids 14, 423–432.

El-Gammal, M., Ahmed, W.H., Ching, C.Y., 2012. Investigation of wall mass transfer characteristics downstream of an orifice. Nucl. Eng. Des. 242, 353–360.

Fujisawa, N., Kanatani, N., Yamagata, T., Takano, T., 2015a. Mechanism of non-axisymmetric pipe-wall thinning in pipeline with elbow and orifice under influence of swirling flow. Nucl. Eng. Des. 285, 126–133.

Fujisawa, N., Yamagata, T., Kanatani, N., Watanabe, R., 2015b. Non-axisymmetric wall-thinning downstream of elbow-orifice pipeline in swirling flow. Ann. Nucl. Energy 80, 356–364.

Hartley, R., Zisserman, A., 2000. Multiple View Geometry in Computer Vision. Cambridge Univ Press, Cambridge.

Heerenbrink, M.K., 2011. Simultaneous PIV and Balance Measurements on a Pitching Aerofoil.

Hudy, L.M., Naguib, A., Humphreys, W.M., 2007. Stochastic estimation of a separated-flow field using wall-pressure-array measurements. Phys. Fluids 19, 024103.

Husain, Z., Hussain, A., 1979. Axisymmetric mixing layer-Influence of the initial and boundary conditions. AIAA J. 17, 48–55.

Hwang, K.M., Jin, T.E., Kim, K.H., 2009. Identification of the relationship between local velocity components and local wall thinning inside carbon steel piping. J. Nucl. Sci. Technol. 46, 469–478.

Johansen, F., 1930a. Flow through pipe orifices at low Reynolds numbers. Proc. R. Soc. Lond. Ser. A Math. Phys. Character 126, 231–245.

Johansen, F., 1930b. The influence of pipe diameter on orifice discharge coefficients. Annu. Rev. Fluid Mech. 149, 679–681.

Kumar, P., Khanna, S., Moholkar, V.S., 2012. Flow regime maps and optimization thereby of hydrodynamic cavitation reactors. AIChE J. 58, 3858–3866.

Massey, B.S., Ward-Smith, J., 1998. Mechanics of Fluids, Seventh ed. CRC Press.

Mishra, C., Peles, Y., 2005. Incompressible and compressible flows through rectangular microorifices entrenched in silicon microchannels. Microelectromech.

Syst. J. 14, 1000–1012.
Morrison, G.L., DeOtte, R.E., Moen, M., Hall, K.R., Holste, J.C., 1990. Beta ratio, swirl and Reynolds number dependence of wall pressure in orifice flowmeters. Flow Meas. Instrum. 1, 269–277.
Morrison, G.L., Deotte, R.E., Nail, G.H., Panak, D.L., 1993. Mean velocity and turbulence fields inside a $\beta = 0.50$ orifice flowmeter. AIChE J. 39, 745–756.
Morrison, G.L., Hauglie, J., DeOtte Jr, R.E., 1995. Beta ratio, axisymmetric flow distortion and swirl effects upon orifice flow meters. Flow Meas. Instrum. 6, 207–216.
Nail, G.H., 1991. A Study of 3-dimensional Flow Through Orifice Meters. Texas A & M University, Texas.
Neal, D.R., Sciacchitano, A., Smith, B.L., Scarano, F., 2015. Collaborative framework for PIV uncertainty quantification: the experimental database. Meas. Sci. Technol. 26, 074003.
Reader-Harris, M., 2015. Orifice Discharge Coefficient, Orifice Plates and Venturi Tubes. Springer, pp. 127–186.
Reis, L., Carvalho, J., Nascimento, M., Rodrigues, L., Dias, F., Sobrinho, P., 2014. Numerical modeling of flow through an industrial burner orifice. Appl. Therm. Eng. 67, 201–213.
Ruderich, R., Fernholz, H.H., 1986. An experimental investigation of a turbulent shear flow with separation, reverse flow, and reattachment. J. Fluid Mech. 163, 283–322.
Sciacchitano, A., Neal, D.R., Smith, B.L., Warner, S.O., Vlachos, P.P., Wieneke, B., Scarano, F., 2015. Collaborative framework for PIV uncertainty quantification: comparative assessment of methods. Meas. Sci. Technol. 26, 074004.
Sciacchitano, A., Wieneke, B., Scarano, F., 2013. PIV uncertainty quantification by image matching. Meas. Sci. Technol. 24, 045302.
Shaaban, S., 2014. Optimization of orifice meter's energy consumption. Chem. Eng. Res. Des. 92, 1005–1015.
Shah, M.S., Joshi, J.B., Kalsi, A.S., Prasad, C.S.R., Shukla, D.S., 2012. Analysis of flow through an orifice meter: CFD simulation. Chem. Eng. Sci. 71, 300–309.
Singh, V., Tharakan, T.J., 2015. Numerical simulations for multi-hole orifice flow meter. Flow Meas. Instrum. 45, 375–383.
Takano, T., Ikarashi, Y., Uchiyama, K., Yamagata, T., Fujisawa, N., 2016. Influence of swirling flow on mass and momentum transfer downstream of a pipe with elbow and orifice. Int. J. Heat Mass Transf. 92, 394–402.
Tihon, J., Legrand, J., Legentilhomme, P., 2001. Near-wall investigation of backward-facing step flows. Exp. Fluids 31, 484–493.
White, F.M., 2011. Fluid Mechanics, 7th ed. McGraw-Hill, New York.
Wieneke, B., 2015. PIV uncertainty quantification from correlation statistics. Meas. Sci. Technol. 26, 074002.
Wieneke, B., Pfeiffer, K., 2010. Adaptive PIV with Variable Interrogation Window Size and Shape.
Wygnanski, I., Fiedler, H., 1969. Some measurements in the self-preserving jet. J. Fluid Mech. 38, 577–612.
Yagi, T., Kamoda, A., Sato, A., Yang, W., Umezu, M., 2009. 3D volume flow visualization for vascular flow modelling using stereo PIV with fluorescent tracer particles. In: Proceedings of the 8th international symposium on particle image velocimetry (PIV 09), Melbourne, Australia.